

Spin-Coated Crystalline Molecular Monolayers for Performance Enhancement in Organic Field-Effect Transistors

Qijing Wang,^{†,‡} Emilio J. Juarez-Perez,[‡] Sai Jiang,[†] Longbin Qiu,[‡] Luis K. Ono,[‡] Toshio Sasaki,[§] Xinran Wang,[†] Yi Shi,[†] Youdou Zheng,[†] Yabing Qi,^{*,‡,¶} and Yun Li^{*,†,¶}

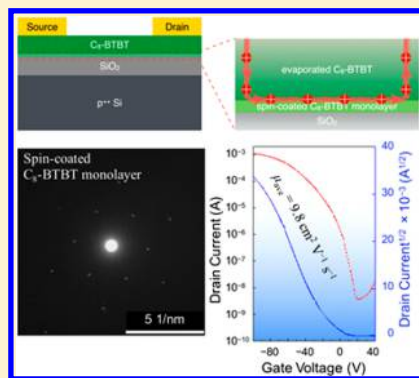
[†]National Laboratory of Solid-State Microstructures, School of Electronic Science and Engineering Collaborative Innovation Center of Advanced Microstructures, Nanjing University, Nanjing 210093, PR China

[‡]Energy Materials and Surface Sciences Unit (EMSSU), Okinawa Institute of Science and Technology Graduate University (OIST), 1919-1 Tancha, Onna-son, Kunigami-gun, Okinawa 904-0495, Japan

[§]Imaging Section, Research Support Division, Okinawa Institute of Science and Technology Graduate University (OIST), 1919-1 Tancha, Onna-son, Kunigami-gun, Okinawa 904-0495, Japan

S Supporting Information

ABSTRACT: In organic field-effect transistors, the first few molecular layers at the semiconductor/dielectric interface are regarded as the active channel for charge transport; thus, great efforts have been devoted to the modification and optimization of molecular packing at such interfaces. Here, we report organic monolayers with large-area uniformity and high crystallinity deposited by an antisolvent-assisted spin-coating method acting as the templating layers between the dielectric and thermally evaporated semiconducting layers. The predeposited crystalline monolayers significantly enhance the film crystallinity of upper layers and the overall performance of transistors using these hybrid-deposited semiconducting films, showing a high carrier mobility up to $11.3 \text{ cm}^2 \text{ V}^{-1} \text{ s}^{-1}$. Additionally, patterned transistor arrays composed of the templating monolayers are fabricated, yielding an average mobility of $7.7 \text{ cm}^2 \text{ V}^{-1} \text{ s}^{-1}$. This work demonstrates a promising method for fabricating low-cost, high-performance, and large-area organic electronics.



Great effort has been devoted to the field of organic field-effect transistors (OFETs) because of their potential applications in low-cost, large-area organic electronics.^{1–5} Charge transport, which determines the device performance, generally occurs at the interfacial layer between a semiconductor and an insulator.^{6–9} Many external factors, such as the dielectric surface roughness, interfacial trap states, and electrostatic interactions between carriers and the dielectric medium, can impede charge transport, leading to the demand for high-quality semiconductor/insulator interfaces. Recently, device performance has been greatly improved by inserting ultrathin polymer films ($\sim 5 \text{ nm}$).^{10,11} This interfacial layer also benefits molecular packing during deposition of the upper layer by acting as a template in a “bottom-up” film growth strategy. In addition, two-dimensional (2D) materials, such as graphene and hexagonal boron nitride (h-BN), with atomic roughness and minimal trap states have been employed as growth templates to obtain organic films with increased crystallinity.^{12–14} While the applications of these materials are often limited by specific substrates, transfer techniques, and crystal sizes, their organic counterparts, i.e., ultrathin molecular monolayers or multilayers that undergo lattice-matched film growth via van der Waals forces (e.g., $\pi-\pi$ interactions) between organic molecules, are the inherent choice for the template layer. However, the deposition of high-quality, large-area, ultrathin organic films remains an essential challenge.

Uniform ultrathin films deposited by physical vapor deposition (PVD)^{15–18} usually contain numerous grain boundaries or are limited by the template size (2D atomic crystals). Additionally, solution-processed monolayers and multilayers^{8,19,20} are normally formed in discontinuous polycrystalline phases, leading to difficulty in large-area practical applications, such as transistor arrays. Therefore, the deposition of highly crystalline organic molecular ultrathin films as an interfacial layer and scalable template is highly desirable.

Antisolvent crystallization has been widely used in perovskite crystal growth by solution process, where the antisolvent can speed up the nucleation and eventually improve the film uniformity.^{21–23} In this work, we propose a new strategy for the growth of crystalline molecular monolayers via an antisolvent-assisted spin-coating method, wherein a continuous and uniform monolayer can be successfully obtained on a large scale. An upper organic layer is then deposited on the monolayers by thermal evaporation, exhibiting enhanced grain size and crystallinity. The OFETs (Figure 1a) based on these hybrid-deposited organic films exhibit a high carrier mobility up to $11.3 \text{ cm}^2 \text{ V}^{-1} \text{ s}^{-1}$, showing much improved device

Received: February 2, 2018

Accepted: March 1, 2018

Published: March 1, 2018



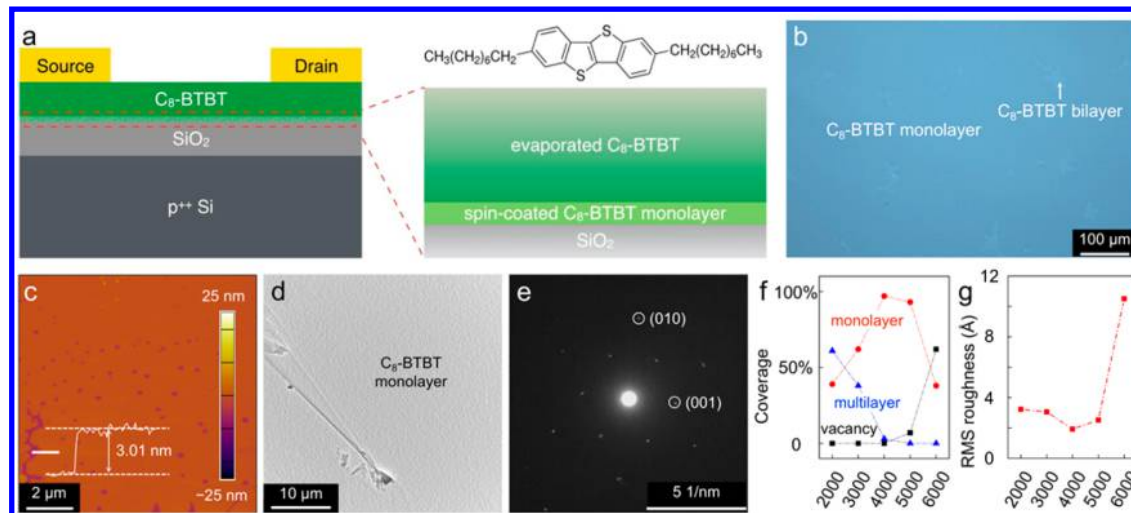


Figure 1. (a) Structure of a bottom-gate top-contact transistor with a spin-coated C₈-BTBT monolayer at the dielectric/semiconductor interface and the molecular structure of C₈-BTBT. (b) Optical microscopy and (c) atomic force microscopy images of the C₈-BTBT monolayer. (d) TEM image of the C₈-BTBT monolayer and (e) its corresponding SAED patterns. (f) Coverage on SiO₂/Si substrate of vacancy, monolayer, and multilayer of spin-coated C₈-BTBT films at various speeds. (g) RMS roughness of the spin-coated monolayers and multilayers based on the AFM images.

performance compared to that without this templating monolayer. Moreover, high-performance transistor arrays are successfully realized by employing the spin-coated monolayer as a template.

Diocetylbenzothienobenzothiophene (C₈-BTBT), a p-type organic semiconductor possessing high carrier mobility and undergoing facile crystallization, was selected for our study.^{24,25} We dissolved C₈-BTBT in a mixed solvent of anisole and *p*-anisaldehyde (0.5 wt %).^{26,27} The solution (60 μL) was first drop-cast onto a SiO₂/Si substrate. Then, the antisolvent, *N,N*-dimethylformamide (DMF), was drop-cast onto the C₈-BTBT solution for the spin-coating process. The experimental procedure is described in further detail in the *Experimental Methods* in the Supporting Information. The substrates were pretreated with phenyltrichlorosilane (PhTS) to reduce the number of interfacial trap states²⁸ and to guarantee a hydrophilic surface for the following solution process. As the solution was pulled by centrifugal force during the spin-coating process, high-quality monolayers were created. The optical microscopy (OM) and atomic force microscopy (AFM) images of the monolayer are shown in Figure 1b,c, and both exhibit high morphologic uniformity and atomic smoothness (root-mean-square (RMS) roughness = 1.95 Å) with a thickness of ~3.01 nm (inset in Figure 1c), close to the *c*-axis unit cell parameter reported for the C₈-BTBT single crystal.²⁹ Almost the entire substrate area (1.5 cm × 1.5 cm) is well covered with C₈-BTBT monolayer, and only a few bilayer islands exist in isolated areas. In addition, the crystallinity of the C₈-BTBT monolayer was examined by transmission electron microscopy (TEM) (Figure 1d) and its corresponding selected area electron diffraction (SAED) (Figure 1e). Clear electron diffraction patterns are observed, indicating a highly ordered molecular packing. Therefore, this spin-coating method is proven to be effective for depositing monolayers over a large area. It is critical to ensure that the C₈-BTBT solution was entirely covered by DMF, which is immiscible with anisole (Figure S1). C₈-BTBT molecules can migrate at this anisole/DMF interface, aggregating through strong π–π interactions and S···C electrostatic interactions between thiophene heterocycles and hydrophobic interaction between the aliphatic C₈

carbon chains forming micella sheets.³⁰ As the spin-coating procedure goes on, the ultrathin crystalline sheets grow equatorially larger and connect together, evolving into large-area monolayers (Figure S2). To adequately study the monolayer deposition, the influence of DMF on the deposition of the C₈-BTBT monolayer was also studied (Figure S3), and the optimal volume of DMF is the same as that of the C₈-BTBT solution (60 μL). We also clarified the effect of the C₈-BTBT concentration on the film morphology (Figure S4) and found 0.5 wt % to be the optimal concentration for monolayer deposition. In particular, we reduced the spin-coating time to 30 s, and some solution remained on the samples at spots where the solvent evaporation process could be observed. The amount of C₈-BTBT in the remaining solution was sufficient to form a uniform monolayer without forming multilayers or redundant islands (Figure S5). Hence, the production of such large-area uniform monolayers is attributed to the limited DMF and C₈-BTBT concentration.

Figure S6 shows the OM images illustrating the film morphology and surface roughness of the ultrathin C₈-BTBT layers at various spin-coating speeds, and their corresponding AFM images are shown in Figure S7. We estimate the coverages of monolayers, multilayers, and vacancies. As shown in Figure 1f, when spin-coating at relatively low speeds of 2000 and 3000 rpm, the coverages of monolayers are ~39% and ~62%, respectively. Dendritic crystalline nuclei and islands as observed in the microscopy images result in the multilayer coverages of ~61% and ~38% for the films spin-coated at 2000 and 3000 rpm, respectively. When depositing at an optimized speed of 4000 rpm, nearly all the substrate (~97%) is covered by monolayers. Further increase in the spin speed causes a highly discontinuous film, containing a large number of small isolated islands. Hence, the area of vacancies on the substrate increases to ~7% and ~62% for the samples deposited at 5000 and 6000 rpm, respectively. The RMS roughness of the spin-coated C₈-BTBT layers first decreased and then sharply increased (6000 rpm) (Figure 1g). In addition, the monolayer spin-coated at 4000 rpm yields the minimal roughness (1.93 Å). The OM images of the C₈-BTBT monolayers/multilayers on a larger scale are shown in Figure S8. Next, TEM measurements

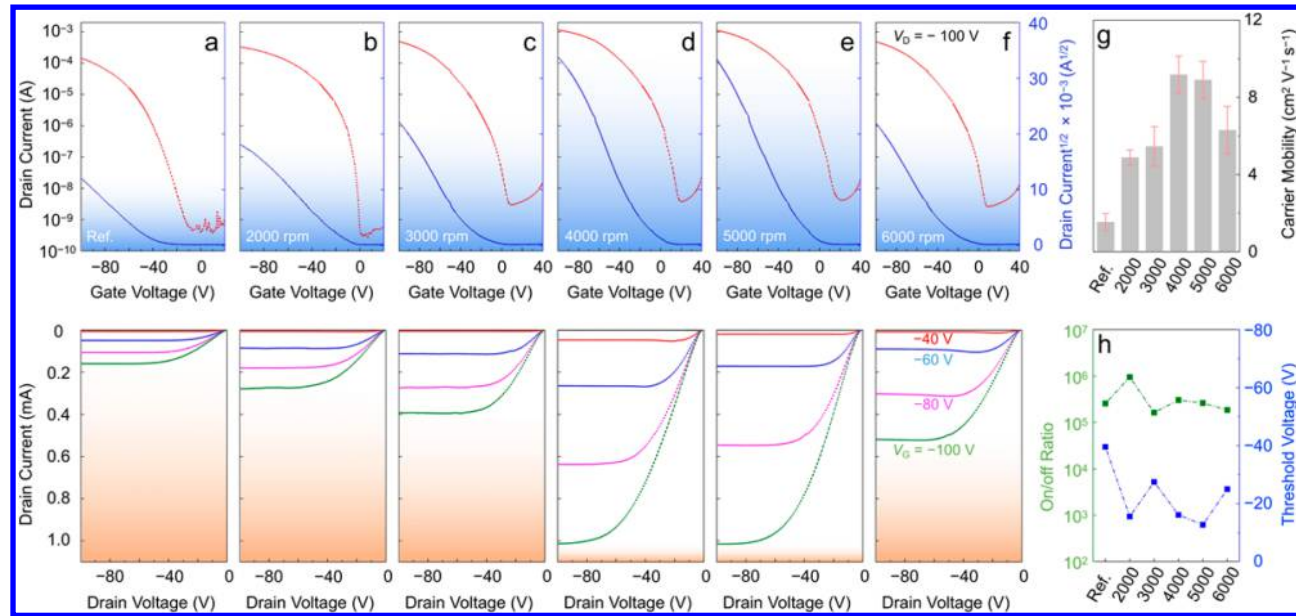


Figure 2. Transistor characteristics of OFETs based on 30 nm thick C₈-BTBT films (a) without and (b–f) with monolayers or multilayers spin-coated at speeds of 2000–6000 rpm. In the output curves, the gate voltage increases from 0 V to –100 V with a step of –20 V. The channel length (L) and width (W) are 250 μm and 1 mm, respectively. (g) OFET mobility along with the (h) on/off ratio and threshold voltage of the transistors based on C₈-BTBT films spin-coated at different speeds.

were employed to further study the film properties of the ultrathin C₈-BTBT films spin-coated at different speeds (insets in Figures S6a–c and S9–11). For comparison, a 3 nm thick evaporated C₈-BTBT thin film was prepared as a reference sample. No diffraction patterns are observed, indicating that the evaporated C₈-BTBT film is highly disordered (Figures S9 and S11a). On the other hand, clear electron diffraction patterns are found for the spin-coated samples (2000, 3000, and 4000 rpm), and the molecular packing and lattice parameters are comparable. These results indicate that the spin-coated ultrathin films have similar crystalline structures (Figure S12). When spin-coating at the speeds of 5000 and 6000 rpm, the C₈-BTBT monolayers will disperse because of the discontinuity of the films and cannot be transferred onto Cu grids. The above results show that our antisolvent-assisted spin-coating method can be used to form highly crystalline molecular monolayers and multilayers.

We indeed examined the transistor behaviors based on the samples only with the spin-coated ultrathin molecular monolayers or multilayers and did not obtain good electrical performances. Thus, after spin-coating the ultrathin films on the substrates, we deposited 27 nm C₈-BTBT films by thermal evaporation to fabricate bottom-gate top-contact (BGTC) transistors. MoO₃ (3 nm) as a buffer layer and Au electrodes (80 nm) were thermally evaporated on the active layer (see Experimental Methods in the Supporting Information). For comparison, devices utilizing totally evaporated films (30 nm) as semiconducting layers were set as reference samples. The channel length and width were 250 μm and 1 mm, respectively. Figure 2a–f shows the typical transfer and output characteristics of the hybrid-deposited C₈-BTBT-based FETs. As shown in Figure 2g, the average carrier mobility (μ_{FET}) of reference devices was 1.5 $\text{cm}^2 \text{V}^{-1} \text{s}^{-1}$ (averaged over 10 devices), which is similar to that in the literature.^{10,31–33} The devices with predeposited ultrathin C₈-BTBT layers exhibited much improved electrical performance, exhibiting a templating effect of the spin-coated crystalline molecular monolayers and

multilayers at the dielectric interfaces. When the initial layers were spin-coated at 2000 and 3000 rpm, the average values of μ_{FET} were 4.9 and 5.5 $\text{cm}^2 \text{V}^{-1} \text{s}^{-1}$, respectively. In addition, the highest average mobility of 9.2 $\text{cm}^2 \text{V}^{-1} \text{s}^{-1}$ was obtained when spin-coating at 4000 rpm. The maximum mobility we obtained was as high as 11.3 $\text{cm}^2 \text{V}^{-1} \text{s}^{-1}$, which is among the highest values (Table S1). The mobility decreases with further increased spin speed. Small changes in the on/off ratio can be observed in Figure 2h, and the threshold voltage of the devices with spin-coated layers is generally lower than that of the reference samples, decreasing from 39.6 to 16.2 V (4000 rpm). The relatively high off currents should be due to the air exposure during the spin-coating and before the evaporation process. The electrical parameters (carrier mobility, on/off ratio, and threshold voltage V_{TH}) are summarized in Table S2.

Considering the enhanced transistor performance using our interfacial C₈-BTBT monolayers, we suggest that the insertion of molecular monolayers or multilayers template at the dielectric interface has a significant influence on all organic semiconducting layers, for example, their crystalline and electronic properties. Therefore, we assessed the crystallinity of C₈-BTBT films using X-ray diffraction (XRD). The spin-coated monolayers were too thin to gain obvious peaks with adequate intensities (Figures S13 and S14). Despite the weak signals, tiny peaks can be observed at $2\theta = 6.2^\circ$ and 9.1° for the samples deposited at speeds of 2000 and 3000 rpm, because these films contain some multilayer structures. Therefore, to evaluate the crystallinity of the spin-coated films and their effect on upper layer deposition, other C₈-BTBT films (3 and 27 nm) were separately evaporated on all the samples, resulting in hybrid-deposited films with total thicknesses of 6 and 30 nm, respectively. The XRD data, shown in Figures 3 and S15, exhibit the same peak positions for all samples with the C₈-BTBT films. The 6 nm thick film containing a monolayer spin-coated at 4000 rpm showed a sharp peak with the highest intensity increasing more than 3-fold compared with that of other samples, and the peak intensity of the other films first

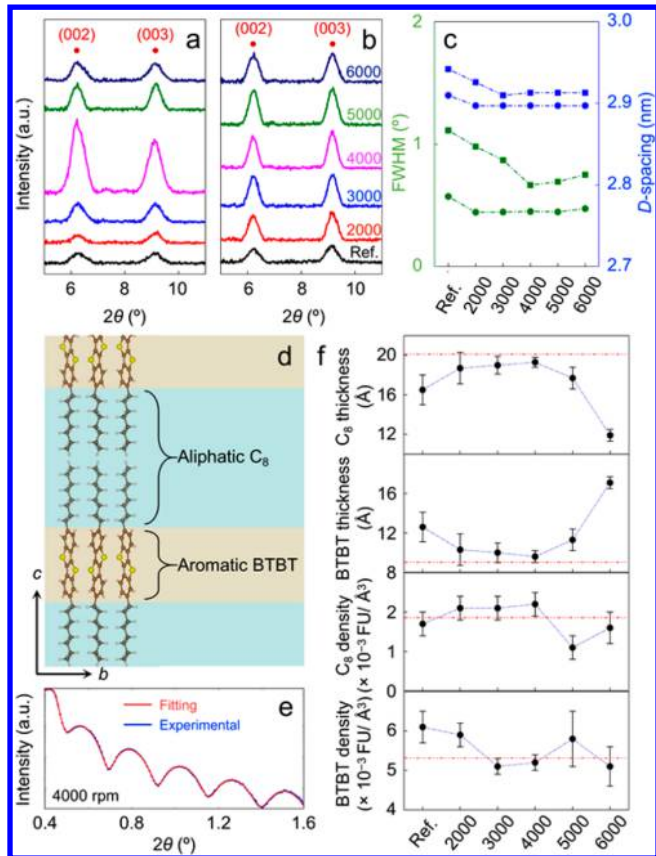


Figure 3. XRD patterns of the C₈-BTBT films with total thicknesses of (a) 6 nm and (b) 30 nm without and with spin-coated monolayers at different speeds. (c) The *d*-spacing (blue) and fwhm (olive) data calculated from the 6 nm thick (squares) and 30 nm thick (circles) films. The films on the reference samples were deposited by thermal evaporation. (d) Detail of the multilayered Si/SiO₂/C₈-BTBT model where C₈-BTBT molecule has been artificially layered in two portions, one consisting of thiophenes (BTBT, pale orange shadow) and aliphatic chains portion (C₈, blue shadow). (e) Experimental XRR and its fitting based on samples using spin-coating at 4000 rpm. (f) Main parameters extracted from the multilayer model: independent C₈ and BTBT layer thickness and density.

increased and then decreased, while all thicker films show similar intensities (Figure S16). In addition to the peak intensities, the *d*-spacing and full width at half-maximum (fwhm) calculated from the (003) diffraction peaks were examined (Figure 3c). The *d*-spacing of the C₈-BTBT films of both thicknesses and the fwhm of the 30 nm thick films first slowly declined and then stabilized. The fwhm of the 6 nm thick films exhibited a more remarkable change, and the fwhm reached a minimum (0.66°) at a speed of 4000 rpm. This indicates that a spin-coated crystalline monolayer leads to enhanced crystallinity of the structure and crystallite size of the upper films (especially the first evaporated monolayer), and this effect is weakened with an increase in the film thickness. The XRD data are summarized in Table S3.

Crystallinity of these hybrid-deposited C₈-BTBT films was further studied using X-ray reflectivity (XRR) from $2\theta = 0.2^\circ$ to 10° accounting for reflection fringes (Figure S17). The XRR profile is analyzed using a multilayered stack model as depicted in Figure 3d. In this model, C₈-BTBT molecules are considered oriented along the *c*-axis perpendicular to the substrate plane forming layers alternating the dense aromatic thiophenes and

less dense aliphatic saturated carbon C₈ hydrocarbon chains. It can be observed that the hybrid-deposited sample prepared using spin-coating at 4000 rpm shows the best fit between experimental and theoretical multilayered models (Figures 3e and S18). Intramolecular layer thicknesses and densities of these samples match well with the experimental thicknesses and densities estimated from the experimental single-crystal structure of C₈-BTBT (Figure 3f and Table S4). Note that molecules in disordered regions should have different molecular orientations and densities from that of well-packed molecules. It can result in values of C₈ and BTBT thicknesses and densities that are either higher or lower than those of single crystal. Therefore, the film crystallinity, as compared with perfectly ordered single crystal, can be efficiently evaluated by examining the deviations from the values of C₈ and BTBT thicknesses and densities for single crystals. As shown in Figure 3f, the samples prepared using spin-coating at 4000 rpm also show very small deviations from single crystal; overall, it can be considered as the most perfect sample both in the short- and long-range probed substrate with lowest reflection fringe height attenuation. In addition, the totally evaporated sample without the predeposited monolayer gives the most disordered thin film for the lack of this template effect. Thus, we conclude that the initial spin-coated C₈-BTBT monolayers possess good crystallinity and act as a template to allow the evaporated C₈-BTBT molecules to arrange into a well-organized order, leading to larger grain sizes, especially in the initial few layers (Figure S19).

To further understand the improved performance of the C₈-BTBT transistors by the crystalline molecular ultrathin templates, we examined the energy levels of the semiconductor (highest occupied molecular orbital (HOMO)) and work function (WF) when using different spin-coating speeds for C₈-BTBT monolayer and multilayer deposition. Ultraviolet photoelectron spectroscopy (UPS) measurements were carried out to investigate the energy levels of the C₈-BTBT films. Figure 4 shows the secondary electron cutoff region, representative of the WF, and the onset of the HOMO. A small shift (~0.2 eV) in the HOMO and WF is found between the spin-coated monolayers and the reference sample. In addition, the ionization potential (IP) shows negligible change (Figure 4b). On the other hand, the energy levels of the thicker films (30 nm) present negligible fluctuations, suggesting that these thick films possess similar surface properties. More details are illustrated in the energy level diagram (Figure S20), which reveals that the upper layers are insusceptible to the bottom spin-coated templating monolayers and multilayers. Hence, the enhanced device performance is attributed to the template effect produced by the first few molecular layers at the semiconductor/dielectric interface.

Encouraged by the performance of individual OFETs and the deposition of large-area high-quality monolayers via this method, we went on to fabricate transistor arrays. For patterning technologies, one feasible strategy is to selectively deposit hydrophilic self-assembly monolayers in the patterned areas, in favor of the deposition of C₈-BTBT monolayers (see the Experimental Section and Figure S21). In the patterned areas (hydrophilic), C₈-BTBT monolayers were deposited as expected (Figure S22). On the basis of the spin-coated monolayers, we further deposited 27 nm C₈-BTBT films by thermal evaporation utilizing shadow masks to obtain hybrid films. The typical transfer characteristics of the array devices are

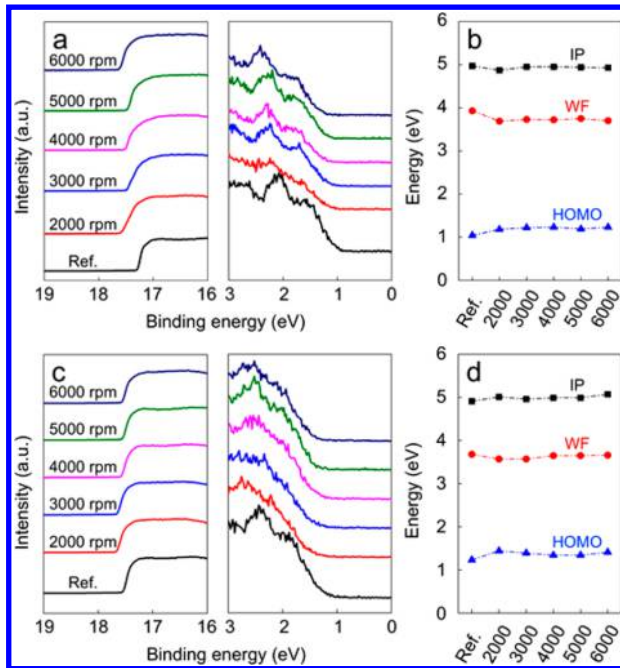


Figure 4. UPS spectra (a) near the cutoff for secondary electron emission (left) and near the HOMO edge (right) for C_8 -BTBT monolayers and multilayers spin-coated at different speeds. (b) Plots of the IP, WF, and HOMO. (c and d) Spectra for the spin-coated C_8 -BTBT monolayers and multilayers and the 27 nm thick evaporated films.

shown in Figure S22c, and the average μ_{FET} is estimated to be $7.7 \text{ cm}^2 \text{ V}^{-1} \text{ s}^{-1}$.

In summary, an antisolvent-assisted spin-coating method is demonstrated for the deposition of C_8 -BTBT monolayers on SiO_2 substrates. In particular, the molecular monolayers spin-coated at a speed of 4000 rpm exhibit atomic smoothness and high uniformity. They also serve as an ideal template for the growth of the upper layer. Transistors based on hybrid-deposited C_8 -BTBT films evaporated on the monolayers and multilayers yielded average and maximum mobilities of 9.8 and $11.3 \text{ cm}^2 \text{ V}^{-1} \text{ s}^{-1}$, respectively. In addition, this method was applied in the fabrication of high-performance transistor arrays. Our work presents an effective templating method by depositing a smooth monolayer on the dielectric layer to produce highly ordered upper layers. During thermal evaporation, C_8 -BTBT molecules can spontaneously pack along with the existing monolayers to obtain an enhanced crystallinity. This method should be extended to other semiconductors and complicated structures, such as heterojunctions.

■ ASSOCIATED CONTENT

S Supporting Information

The Supporting Information is available free of charge on the ACS Publications website at DOI: [10.1021/acs.jpcllett.8b00352](https://doi.org/10.1021/acs.jpcllett.8b00352).

Further details about morphological properties, crystalline properties, energy level diagram, and patterned transistor arrays ([PDF](#))

■ AUTHOR INFORMATION

Corresponding Authors

*E-mail: yli@nju.edu.cn.

*E-mail: Yabing.Qi@OIST.jp.

ORCID

Xinran Wang: [0000-0002-3975-1667](https://orcid.org/0000-0002-3975-1667)

Yabing Qi: [0000-0002-4876-8049](https://orcid.org/0000-0002-4876-8049)

Yun Li: [0000-0003-1753-7317](https://orcid.org/0000-0003-1753-7317)

Author Contributions

Y.L. and Y.Q. conceived the idea and initiated and supervised the work. Q.W. designed, implemented, and optimized the hybrid deposition of C_8 -BTBT films and device fabrication. E.J.J.-P. performed the XRR measurements, multilayered modeling, and its analysis. L.Q. and L.K.O. contributed to XRD and UPS measurements and analysis. All authors reviewed and revised the manuscript.

Notes

The authors declare no competing financial interest.

■ ACKNOWLEDGMENTS

This work was supported by NSFC under Grant Nos. 61774080 and 61574047; NSFJS under Grant No. BK20170075; and funding from the Energy Materials and Surface Sciences Unit of the Okinawa Institute of Science and Technology Graduate University, the OIST R&D Cluster Research Program, the OIST Proof of Concept (POC) Program.

■ REFERENCES

- Mohammadi, E.; Zhao, C.; Meng, Y.; Qu, G.; Zhang, F.; Zhao, X.; Mei, J.; Zuo, J.-M.; Shukla, D.; Diao, Y. Dynamic-Template-Directed Multiscale Assembly for Large-Area Coating of Highly-Aligned Conjugated Polymer Thin Films. *Nat. Commun.* **2017**, *8*, 16070.
- Giri, G.; Li, R.; Smilgies, D.-M.; Li, E. Q.; Diao, Y.; Lenn, K. M.; Chiu, M.; Lin, D. W.; Allen, R.; Reinschach, J.; et al. One-Dimensional Self-Confinement Promotes Polymorph Selection in Large-Area Organic Semiconductor Thin Films. *Nat. Commun.* **2014**, *5*, 3573.
- Lee, B. H.; Hsu, B. B. Y.; Patel, S. N.; Labram, J.; Luo, C.; Bazan, G. C.; Heeger, A. J. Flexible Organic Transistors with Controlled Nanomorphology. *Nano Lett.* **2016**, *16*, 314–319.
- Moon, H.; Seong, H.; Shin, W. C.; Park, W.-T.; Kim, M.; Lee, S.; Bong, J. H.; Noh, Y.-Y.; Cho, B. J.; Yoo, S.; et al. Synthesis of Ultrathin Polymer Insulating Layers by Initiated Chemical Vapour Deposition for Low-Power Soft Electronics. *Nat. Mater.* **2015**, *14*, 628–635.
- Liu, C.; Xu, Y.; Noh, Y.-Y. Contact Engineering in Organic Field-Effect Transistors. *Mater. Today* **2015**, *18*, 79–96.
- Brondijk, J. J.; Roelofs, W. S. C.; Mathijssen, S. G. J.; Shehu, A.; Cramer, T.; Biscarini, F.; Blom, P. W. M.; de Leeuw, D. M. Two-Dimensional Charge Transport in Disordered Organic Semiconductors. *Phys. Rev. Lett.* **2012**, *109*, 056601.
- Kronemeijer, A. J.; Pecunia, V.; Venkateshvaran, D.; Nikolla, M.; Sadhanala, A.; Moriarty, J.; Szumilo, M.; Sirringhaus, H. Two-Dimensional Carrier Distribution in Top-Gate Polymer Field-Effect Transistors: Correlation Between Width of Density of Localized States and Urbach Energy. *Adv. Mater.* **2014**, *26*, 728–733.
- Zhang, F.; Di, C.-A.; Berdunov, N.; Hu, Y.; Hu, Y.; Gao, X.; Meng, Q.; Sirringhaus, H.; Zhu, D. Ultrathin Film Organic Transistors: Precise Control of Semiconductor Thickness via Spin-Coating. *Adv. Mater.* **2013**, *25*, 1401–1407.
- Liu, C.; Li, G.; Di Pietro, R.; Huang, J.; Noh, Y.-Y.; Liu, X.; Minari, T. Device Physics of Contact Issues for the Overestimation and Underestimation of Carrier Mobility in Field-Effect Transistors. *Phys. Rev. Appl.* **2017**, *8*, 034020.
- Sun, H.; Wang, Q.; Li, Y.; Lin, Y.-F.; Wang, Y.; Yin, Y.; Xu, Y.; Liu, C.; Tsukagoshi, K.; Pan, L.; et al. Boost Up Carrier Mobility for Ferroelectric Organic Transistor Memory via Buffering Interfacial Polarization Fluctuation. *Sci. Rep.* **2015**, *4*, 7227.
- Yokota, T.; Kajitani, T.; Shidachi, R.; Tokuhara, T.; Kaltenbrunner, M.; Shoji, Y.; Ishiware, F.; Sekitani, T.; Fukushima, T.; Someya, T. A Few-Layer Molecular Film on Polymer Substrates to

- Enhance the Performance of Organic Devices. *Nat. Nanotechnol.* **2018**, *13*, 139.
- (12) Kim, K.; Santos, E. J. G.; Lee, T. H.; Nishi, Y.; Bao, Z. Epitaxially Grown Strained Pentacene Thin Film on Graphene Membrane. *Small* **2015**, *11*, 2037–2043.
- (13) Kim, K.; Lee, T. H.; Santos, E. J. G.; Jo, P. S.; Salleo, A.; Nishi, Y.; Bao, Z. Structural and Electrical Investigation of C 60–Graphene Vertical Heterostructures. *ACS Nano* **2015**, *9*, 5922–5928.
- (14) Lee, T. H.; Kim, K.; Kim, G.; Park, H. J.; Scullion, D.; Shaw, L.; Kim, M.-G.; Gu, X.; Bae, W.-G.; Santos, E. J. G.; et al. Chemical Vapor-Deposited Hexagonal Boron Nitride as a Scalable Template for High-Performance Organic Field-Effect Transistors. *Chem. Mater.* **2017**, *29*, 2341–2347.
- (15) Zhang, Y.; Qiao, J.; Gao, S.; Hu, F.; He, D.; Wu, B.; Yang, Z.; Xu, B.; Li, Y.; Shi, Y.; et al. Probing Carrier Transport and Structure-Property Relationship of Highly Ordered Organic Semiconductors at the Two-Dimensional Limit. *Phys. Rev. Lett.* **2016**, *116*, 016602.
- (16) Tello, M.; Chiesa, M.; Duffy, C. M.; Sirringhaus, H. Charge Trapping in Intergrain Regions of Pentacene Thin Film Transistors. *Adv. Funct. Mater.* **2008**, *18*, 3907–3913.
- (17) Gundlach, D. J.; Nichols, J. A.; Zhou, L.; Jackson, T. N. Thin-Film Transistors Based on Well-Ordered Thermally Evaporated Naphthacene Films. *Appl. Phys. Lett.* **2002**, *80*, 2925–2927.
- (18) Wu, B.; Zhao, Y.; Nan, H.; Yang, Z.; Zhang, Y.; Zhao, H.; He, D.; Jiang, Z.; Liu, X.; Li, Y.; et al. Precise, Self-Limited Epitaxy of Ultrathin Organic Semiconductors and Heterojunctions Tailored by Van Der Waals Interactions. *Nano Lett.* **2016**, *16*, 3754–3759.
- (19) Chen, H.; Dong, S.; Bai, M.; Cheng, N.; Wang, H.; Li, M.; Du, H.; Hu, S.; Yang, Y.; Yang, T.; et al. Solution-Processable, Low-Voltage, and High-Performance Monolayer Field-Effect Transistors with Aqueous Stability and High Sensitivity. *Adv. Mater.* **2015**, *27*, 2113–2120.
- (20) Shan, L.; Liu, D.; Li, H.; Xu, X.; Shan, B.; Xu, J.-B.; Miao, Q. Monolayer Field-Effect Transistors of Nonplanar Organic Semiconductors with Brickwork Arrangement. *Adv. Mater.* **2015**, *27*, 3418–3423.
- (21) Paek, S.; Schouwink, P.; Athanasopoulou, E. N.; Cho, K. T.; Grancini, G.; Lee, Y.; Zhang, Y.; Stellacci, F.; Nazeeruddin, M. K.; Gao, P. From Nano- to Micrometer Scale: the Role of Antisolvent Treatment on High Performance Perovskite Solar Cells. *Chem. Mater.* **2017**, *29*, 3490–3498.
- (22) Huang, F.; Pascoe, A. R.; Wu, W.-Q.; Ku, Z.; Peng, Y.; Zhong, J.; Caruso, R. A.; Cheng, Y.-B. Effect of the Microstructure of the Functional Layers on the Efficiency of Perovskite Solar Cells. *Adv. Mater.* **2017**, *29*, 1601715–10.
- (23) Wu, Y.; Xie, F.; Chen, H.; Yang, X.; Su, H.; Cai, M.; Zhou, Z.; Noda, T.; Han, L. Thermally Stable MAPbI₃Perovskite Solar Cells with Efficiency of 19.19% and Area Over 1 Cm²achieved by Additive Engineering. *Adv. Mater.* **2017**, *29*, 1701073–1701078.
- (24) Minemawari, H.; Yamada, T.; Matsui, H.; Tsutsumi, J.; Haas, S.; Chiba, R.; Kumai, R.; Hasegawa, T. Inkjet Printing of Single-Crystal Films. *Nature* **2011**, *475*, 364–367.
- (25) Li, Y.; Liu, C.; Kumatai, A.; Darmawan, P.; Minari, T.; Tsukagoshi, K. Patterning Solution-Processed Organic Single-Crystal Transistors with High Device Performance. *AIP Adv.* **2011**, *1*, 022149–7.
- (26) Wang, Q.; Qian, J.; Li, Y.; Zhang, Y.; He, D.; Jiang, S.; Wang, Y.; Wang, X.; Pan, L.; Wang, J.; et al. 2D Single-Crystalline Molecular Semiconductors with Precise Layer Definition Achieved by Floating-Coffee-Ring-Driven Assembly. *Adv. Funct. Mater.* **2016**, *26*, 3191–3198.
- (27) Wang, Q.; Jiang, S.; Qian, J.; Song, L.; Zhang, L.; Zhang, Y.; Zhang, Y.; Wang, Y.; Wang, X.; Shi, Y.; et al. Low-Voltage, High-Performance Organic Field-Effect Transistors Based on 2D Crystalline Molecular Semiconductors. *Sci. Rep.* **2017**, *7*, 7830.
- (28) Giri, G.; Verploegen, E.; Mannsfeld, S. C. B.; Atahan-Evrenk, S.; Kim, D. H.; Lee, S. Y.; Becerril, H. A.; Aspuru-Guzik, A.; Toney, M. F.; Bao, Z. Tuning Charge Transport in Solution-Sheared Organic Semiconductors Using Lattice Strain. *Nature* **2011**, *480*, 504–508.
- (29) Izawa, T.; Miyazaki, E.; Takimiya, K. Molecular Ordering of High-Performance Soluble Molecular Semiconductors and Re-Evaluation of Their Field-Effect Transistor Characteristics. *Adv. Mater.* **2008**, *20*, 3388–3392.
- (30) Xu, C.; He, P.; Liu, J.; Cui, A.; Dong, H.; Zhen, Y.; Chen, W.; Hu, W. A General Method for Growing Two-Dimensional Crystals of Organic Semiconductors by “Solution Epitaxy. *Angew. Chem.* **2016**, *128*, 9671–9675.
- (31) Kano, M.; Minari, T.; Tsukagoshi, K. Improvement of Subthreshold Current Transport by Contact Interface Modification in P-Type Organic Field-Effect Transistors. *Appl. Phys. Lett.* **2009**, *94*, 143304–3.
- (32) Minari, T.; Darmawan, P.; Liu, C.; Li, Y.; Xu, Y.; Tsukagoshi, K. Highly Enhanced Charge Injection in Thienoacene-Based Organic Field-Effect Transistors with Chemically Doped Contact. *Appl. Phys. Lett.* **2012**, *100*, 093303–093305.
- (33) Darmawan, P.; Minari, T.; Xu, Y.; Li, S.-L.; Song, H.; Chan, M.; Tsukagoshi, K. Optimal Structure for High-Performance and Low-Contact-Resistance Organic Field-Effect Transistors Using Contact-Doped Coplanar and Pseudo-Staggered Device Architectures. *Adv. Funct. Mater.* **2012**, *22*, 4577–4583.

Supporting Information

Spin-Coated Crystalline Molecular Monolayers for Performance Enhancement in Organic Field-Effect Transistors

Qijing Wang,^{†,‡} Emilio J. Juarez-Perez,[‡] Sai Jiang,[†] Longbin Qiu,[‡] Luis K. Ono,[‡] Toshio Sasaki,^ξ Xinran Wang,[†] Yi Shi,[†] Youdou Zheng,[†] Yabing Qi,[‡] Yun Li*[†]*

[†]National Laboratory of Solid-State Microstructures School of Electronic Science and Engineering Collaborative Innovation Center of Advanced Microstructures Nanjing University Nanjing 210093, P. R. China

[‡]Energy Materials and Surface Sciences Unit (EMSSU), Okinawa Institute of Science and Technology Graduate University (OIST) 1919-1 Tancha, Onna-son, Kunigami-gun, Okinawa, 904-0495, Japan

^ξImaging Section, Research Support Division, Okinawa Institute of Science and Technology Graduate University (OIST) 1919-1 Tancha, Onna-son, Kunigami-gun, Okinawa, 904-0495, Japan

Corresponding Author

*E-mail: yli@nju.edu.cn; Yabing.Qi@OIST.jp

Experimental Methods

Substrate preparation: Heavily doped p-type silicon wafers with 300 nm-thick thermally grown oxide were used as the substrates. The substrates ($1.5 \times 1.5 \text{ cm}^2$) were sequentially cleaned by sonication in acetone and isopropanol for 8 min each and then treated by UV-ozone for 15 min. For phenyltrichlorosilane (PhTS) treatment, the substrates were immersed into a toluene solution containing PhTS (3 wt%) and heated at 90 °C for 15 hours in a glove box (N₂). To obtain patterned samples, the substrates were first modified by octadecyltrichlorosilane (OTS), then treated by UV-ozone with a shadow mask and finally treated with PhTS. The schematic is shown in Figure S20. For OTS treatment, the substrates were immersed into a chloroform solution containing OTS (3 wt%) for 4 hours.

Deposition of C₈-BTBT films: The p-type organic semiconductor C₈-BTBT (99%) was purchased from Sigma-Aldrich and used without further purification. Solutions with different C₈-BTBT concentrations (0.2, 0.5 and 1.0 wt%) were prepared in mixed solutions of anisole and *p*-anisaldehyde (0.5 wt%). Next, 60 μL of both the C₈-BTBT solution and DMF were sequentially cast on the substrates through pipettes and then spin-coated at different speeds (2000 ~ 6000 rpm) for 60 s to obtain the initial C₈-BTBT multilayers. After that, C₈-BTBT powder was thermally evaporated on these substrates in the same batch at a rate of 0.1 Å s⁻¹ with a base pressure of $\sim 10^{-4}$ Pa.

Characterization of the C₈-BTBT films: An Olympus BX51 optical microscope was used to obtain the OM images. The surface morphology was analysed by AFM (Asylum Research MFP-3D) in tapping mode. The binding energy was characterized by UPS (Kratos AXIS ULTRA HAS, He-Iα = 21.22 eV). The samples were deposited on bare silicon (p++) substrates treated

by UV-ozone to form an ultrathin SiO₂ layer (~2.6 nm), and other parameters were set to be the same as those used during monolayer deposition. XRD and XRR was performed with a Bruker D8 Discover instrument (Bruker AXS K. K.) with Cu K_α source X-rays and experimental data was fitted using the GenX 2.4.10 software (v.2.4.10, <http://genx.sf.net>).³² TEM measurements were carried out by JEM1230R transmission electron microscope (JEOL), and the evaporated films were directly deposited on carbon-coated Cu grids (#36), and the spin-coated monolayers were prepared on mica treated by UV-ozone, which was easy to delaminate for transfer to the carbon-coated Cu grids (#36).

Fabrication and electrical measurements of the FETs: BGTC FETs were fabricated on substrates with C₈-BTBT films through a shadow mask. MoO₃ (3 nm) was used as a buffer layer and deposited on the active layer at a rate of 0.1 Å s⁻¹. Au electrodes (80 nm) were thermally evaporated on the initial 5 nm-thick films at a deposition speed of 0.1 Å s⁻¹ and then at a speed of 0.2 Å s⁻¹. Electrical measurements were performed using a Keithley 4200 semiconductor parameter analyser in a probe station with a base pressure of ~10⁻⁴ Torr. The saturation region equation [$I_{DS} = \mu_{FET}C_i (W/2L) (V_G - V_{TH})^2$] was applied for calculation of the carrier mobility.

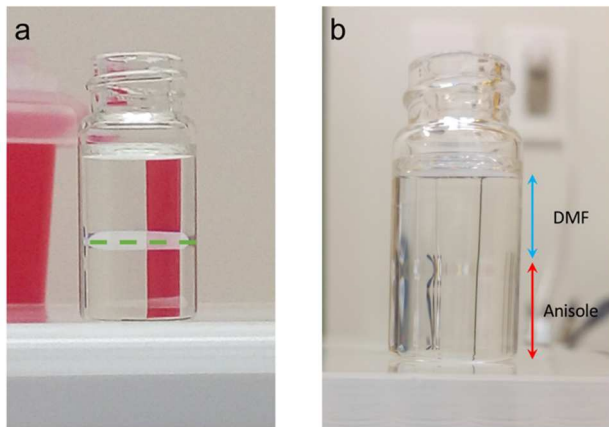


Figure S1. The separation of anisole and DMF. When the two anisole and DMF solutions were mixed, they spontaneously separated which suggests that they are immiscible. The DMF solution (upper one) showed unique photometric characteristics. The density of anisole is 0.99 g/mL, and the density of DMF is 0.94 g/mL. Thus, during the spin-coating process, DMF covers the anisole solution.

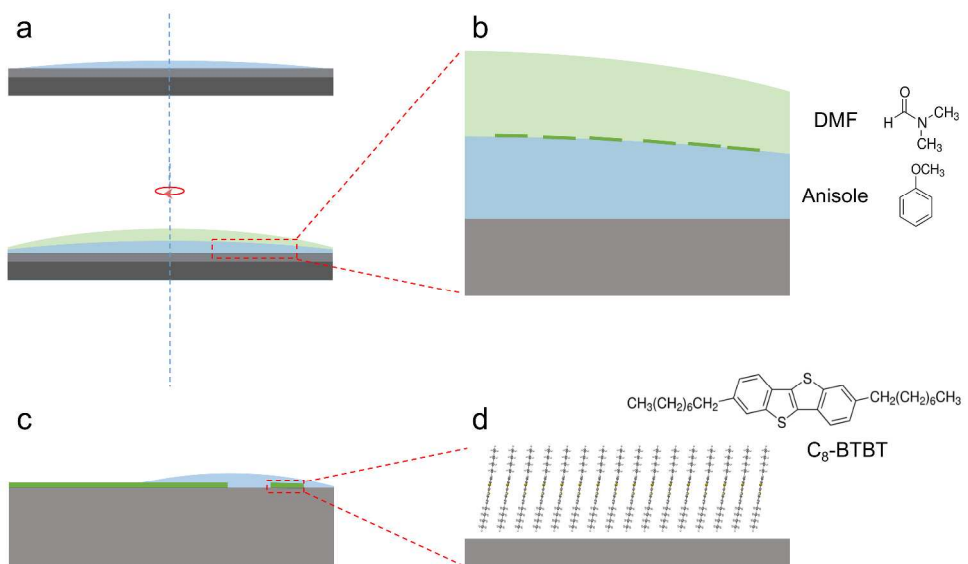


Figure S2. Schematic diagram of the antisolvent-assisted spin-coating deposition of C₈-BTBT thin films.

Both 60 μL C₈-BTBT solution and DMF were casted to the substrates through pipettes sequentially (Figure S2a). At the anisole and DMF interface, C₈-BTBT molecules began to aggregate through strong $\pi-\pi$ interactions and formed ultrathin crystalline sheets (Figure S2b). As the spin-coating procedure went on, the crystalline sheets grew larger and connected together, evolving into large-area monolayers (Figure S2c and d).

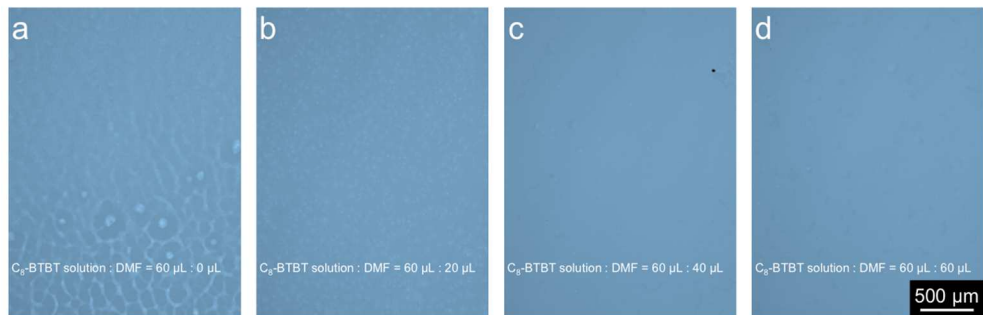


Figure S3. Optical microscopy images of C₈-BTBT films deposited from solutions with different DMF volumes of 0, 20, 40 and 60 μL .

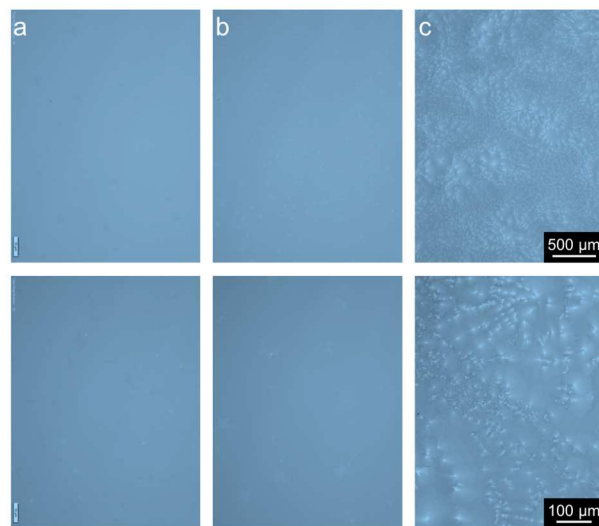


Figure S4. Optical microscopy images of C₈-BTBT films deposited from solutions with different C₈-BTBT concentrations of a-c) 0.25, 0.5 and 1.0 wt%.

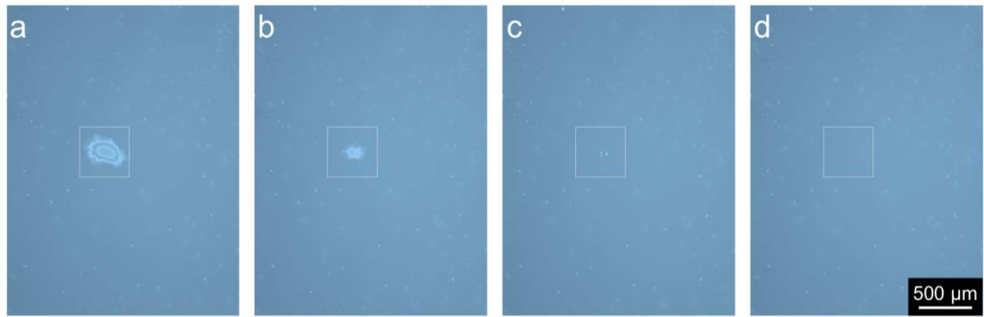


Figure S5. Optical microscopy images of the evaporation of residual solution at different periods after the spin-coating process. The interval between two images is ~10 s.

We investigated the deposition of C₈-BTBT films from solutions with different C₈-BTBT concentrations (0.25, 0.5 and 1.0 wt%). The C₈-BTBT films from 0.25 wt% solutions contain many cracks and pinholes, showing them to be discontinuous (**Figure S4a**). The C₈-BTBT films formed from 1.0 wt% solutions mainly contain multilayers and exhibit a nonuniform surface (**Figure S4c**).

To study the deposition process, we captured optical microscopy images of the evaporation of residual solution (**Figure S5**). After spin-coating for 30 s, there was little solution left on the substrate. We found that the amount of C₈-BTBT in the residual solution was sufficient to form uniform monolayers without generating redundant islands.

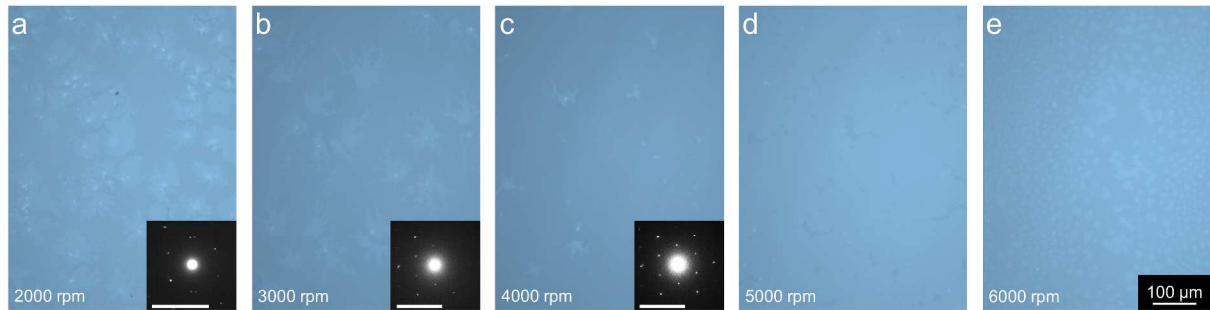


Figure S6. Morphologic properties of the C₈-BTBT films spin-coated on SiO₂/Si substrates. a-e) Optical microscopy images of the C₈-BTBT monolayers/multilayers deposited by spin-coating at 2000 ~ 6000 rpm for 60 s. The insets show their corresponding SAED patterns. Scale bar = 5 nm⁻¹.

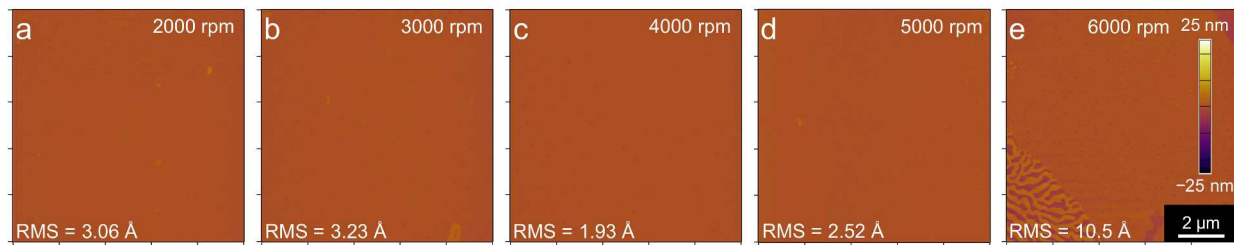


Figure S7. Morphological properties of C₈-BTBT films on SiO₂/Si substrates. a-e) AFM images of C₈-BTBT films deposited by spin-coating at 2000 ~ 6000 rpm for 60 s. f) RMS roughness of the spin-coated monolayers/multilayers.

Based on the performance improvement of OFETs utilizing monolayer/multilayer spin-coated films, we concluded that the spin-coated films play a crucial impact on the upper film growth. Film coverage of monolayer and multilayer were calculated from the OM images (**Figure S6**). The area of multilayer decreased from more than 60% to around 0% along with the increasing speeds while the vacancy presented an opposite trend. Besides, the monolayer coverage showed a first increased then decreased trend and reached a maximum at 4000 rpm.

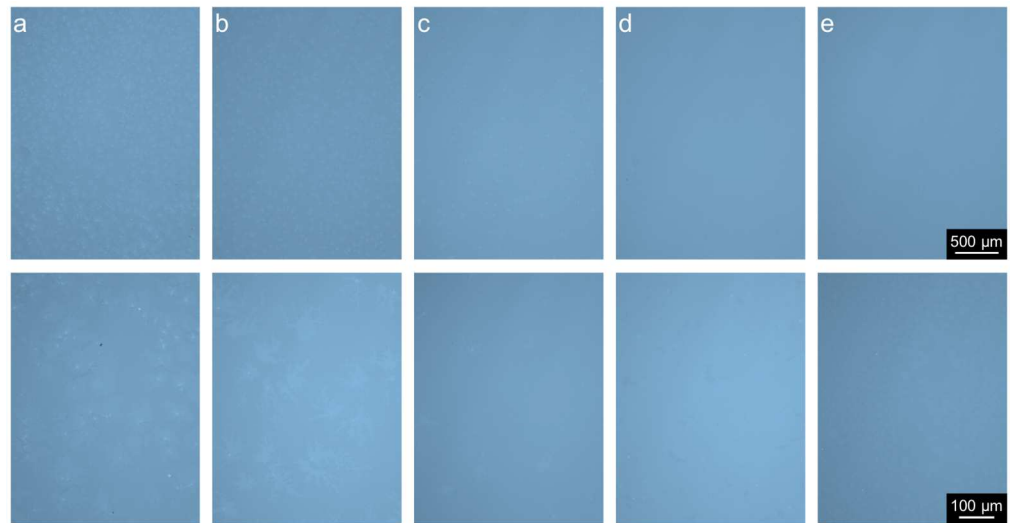


Figure S8. Large-scale optical microscopy images of C₈-BTBT films deposited by spin-coating at 2000 ~ 6000 rpm for 60 s.

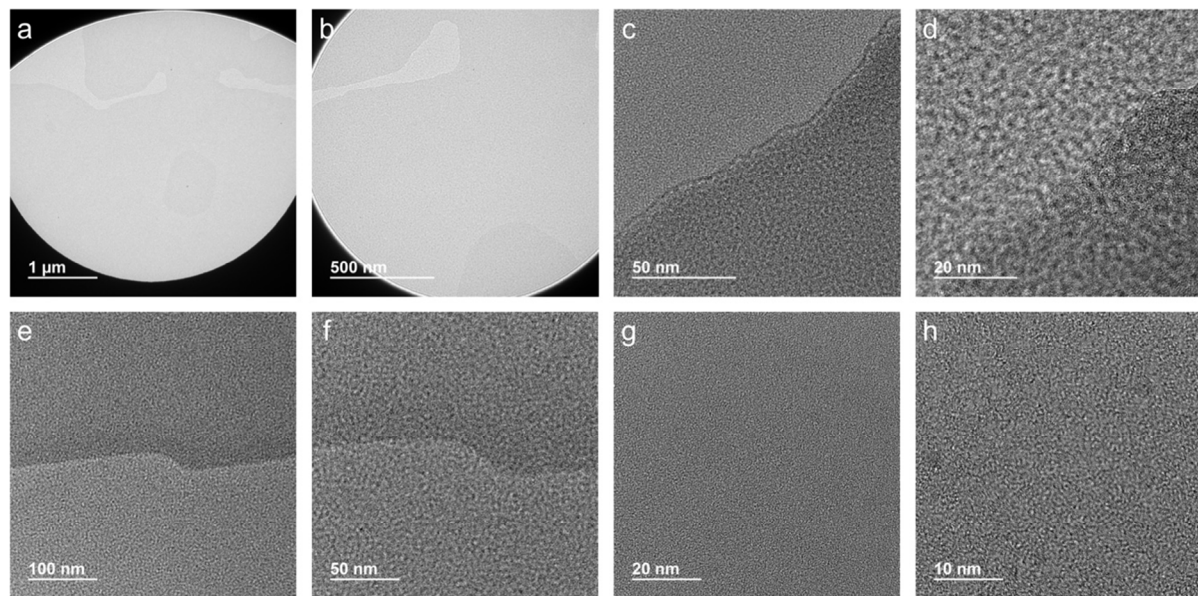


Figure S9. TEM images of evaporated C₈-BTBT monolayers/multilayers on carbon films.

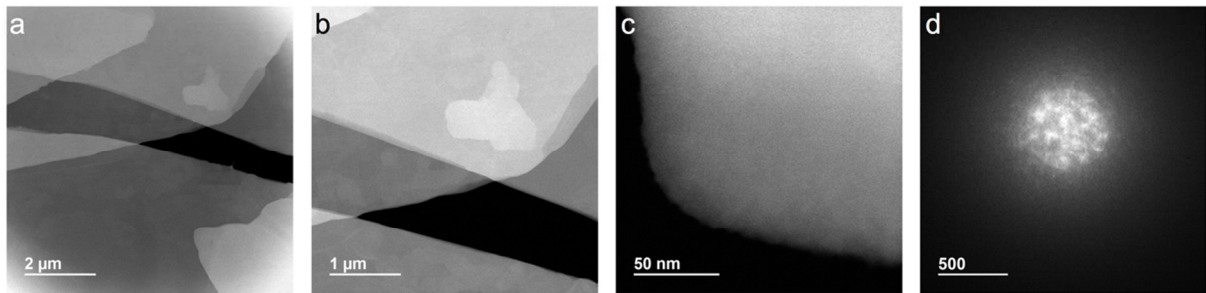


Figure S10. STEM images of spin-coated C₈-BTBT monolayers deposited on Cu grids.

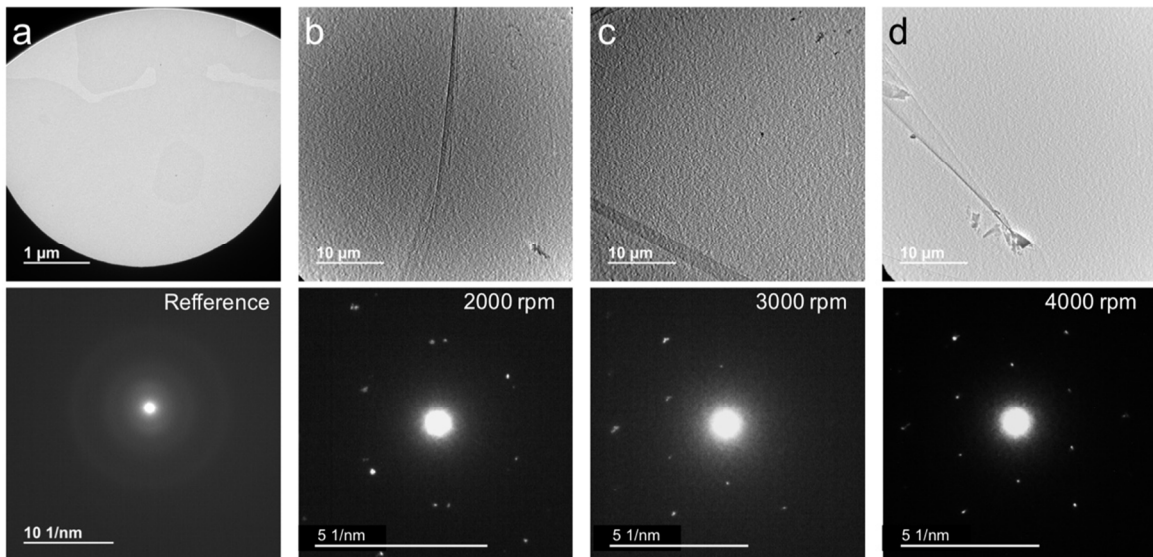


Figure S11. TEM and SAED images of a) evaporated and b-d) spin-coated monolayers/multilayers at speeds of 2000 rpm, 3000 rpm and 4000 rpm.

We further examined the film crystallinity and molecular packing of the C₈-BTBT monolayers/multilayers by transmission electron microscopy (TEM) (**Figure S9**). The C₈-BTBT ultrathin films must be deposited on specific holders for the TEM measurements. Here, we transferred the films to carbon-coated Cu grids (#36). Uniform monolayers, with a small bilayer, can be observed in Figure S9a. Under high magnification, an obvious boundary line can be seen in Figure S9c, e and f, corresponding to different areas of the monolayer. The small “particles” resulted from interference between the electrons and C₈-BTBT molecules. However, no selected

area electron diffraction (SAED) patterns were obtained during the measurements. Thus, we considered this C₈-BTBT film to be in the amorphous phase instead of a crystallized phase, which was also confirmed by the XRD measurements.

The spin-coated C₈-BTBT monolayers/multilayers were deposited on mica substrates, which are formed from the same material, silicon oxide, in a different phase and were also treated by UV-ozone to ensure the same hydrophilicity. Then, the samples were immersed in deionized water to separate the monolayer from the mica substrates for transfer to the Cu grids (#36). Interestingly, monolayers spin-coated at high speed (> 4000 rpm) dispersed in the water and disappeared. Thus, we chose the monolayers spin-coated at a speed of 3000 rpm for the scanning tunneling electron microscopy (STEM) measurements. Here, STEM mode was selected because in TEM mode, the monolayers would be damaged and tend to disappear immediately once exposed to the electron beam. The C₈-BTBT monolayers sometimes overlapped during the transfer operation (**Figure S10**). Figure S10d shows the electron diffraction of the C₈-BTBT monolayers, indicating their good film crystallinity. Thus, a carbon film was coated on the Cu grids, and the C₈-BTBT monolayers/multilayers spin-coated at speeds of 2000 rpm, 3000 rpm and 4000 rpm were transferred to the carbon films (**Figure S11**). Evaporated ultrathin films samples were used as the reference samples. Obvious electron diffraction patterns were found, shown in Figure S10b-d, indicating that the spin-coated monolayers/multilayers were well crystallized, while the evaporated films were in the amorphous phase.

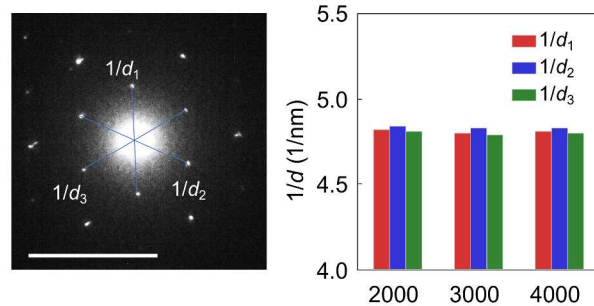


Figure S12. Distance between pattern spots representing d -spacing calculated based on TEM and SAED data.

Based on their corresponding SAED patterns, we calculated the distance between pattern spots representing d -spacing, and negligible changes were observed, indicating the spin-coated ultrathin films have similar crystalline structures.

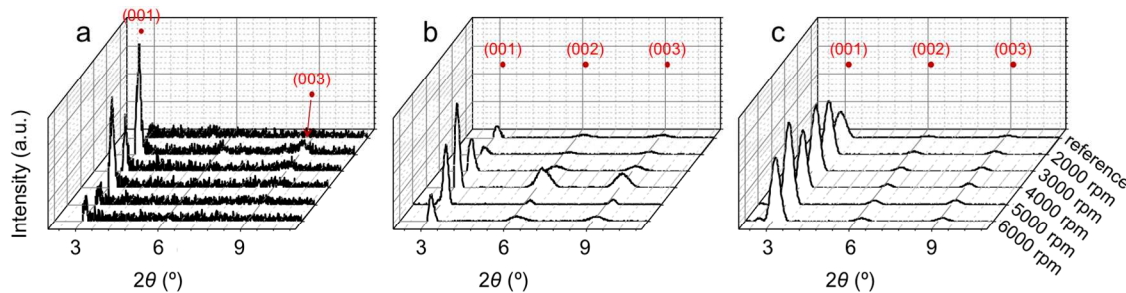


Figure S13. XRD patterns of the evaporated (reference) and spin-coated C₈-BTBT films at different speeds. a) Spin-coated monolayers/multilayers (total thickness of ~3 nm). b) Spin-coated monolayers/multilayers with 3 nm-thick evaporated films (total thickness of ~6 nm). c) Spin-coated monolayers/multilayers with 27 nm-thick evaporated films (total thickness of ~30 nm). C₈-BTBT films were deposited on the reference samples *via* thermal evaporation without spin-coated monolayers/multilayers.

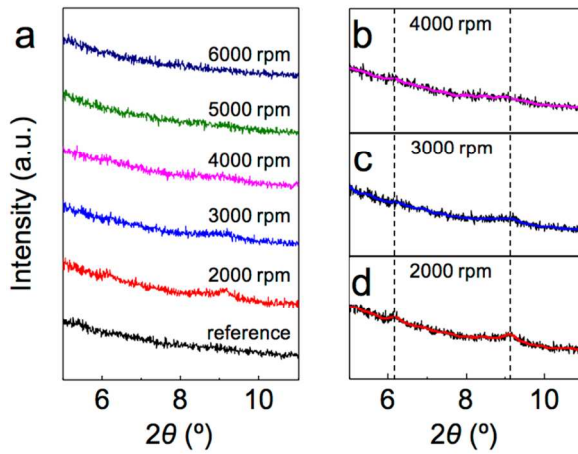


Figure S14. XRD patterns of evaporated (reference) and spin-coated C₈-BTBT films at different speeds.

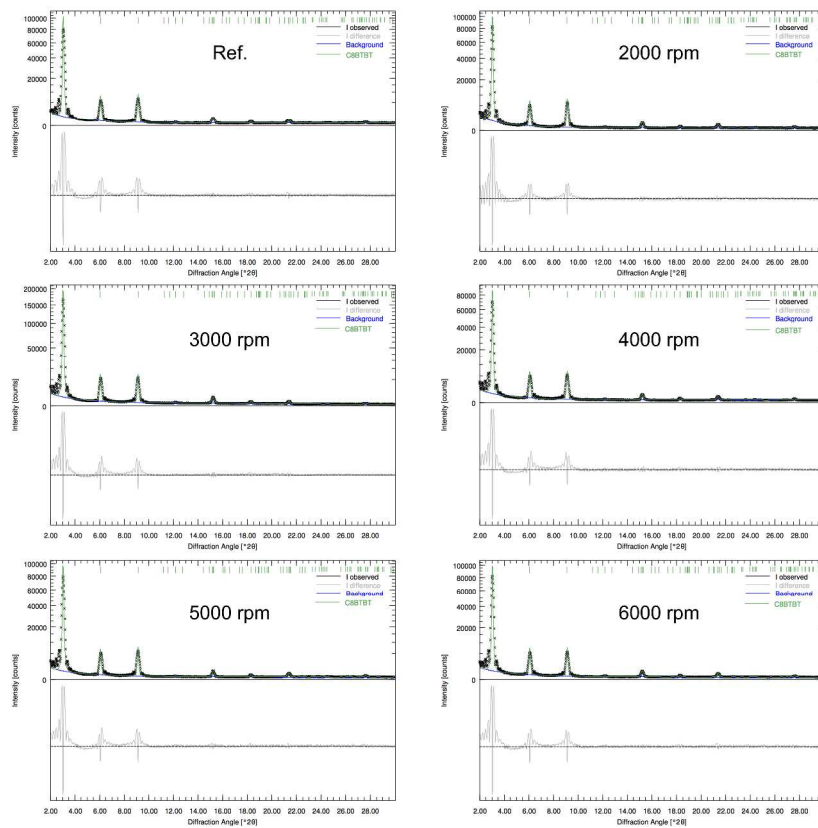


Figure S15. Experimental and theoretical fitting of XRD for reference sample (only evaporated) and samples (30 nm) including predeposited spin coating layer at 2000-6000 rpm.

The evaporated C₈-BTBT films with a thickness of 3 nm (monolayer) do not exhibit obvious peaks for two main reasons. First, the film is too thin to generate enough signal for the detectors; second, this layer has poor crystallinity. In regard to the spin-coated films, however, some small peaks ($2\theta = 6.2^\circ$ and 9.1°) could be seen for the films spin-coated at 2000 and 3000 rpm. We found that these films were continuous and some C₈-BTBT bilayers existed, which contributed to the XRD patterns in **Figure S14b-d**. In addition, the films deposited at high speeds showed a discontinuous morphology, and no peaks could be found. Furthermore, lattice constants of these hybrid-deposited C₈-BTBT films were also calculated from the XRD data (**Figure S15** and **Table S3**). It is clearly observed that 4000 rpm-spin-coated C₈-BTBT film exhibits the most compact molecular packing.

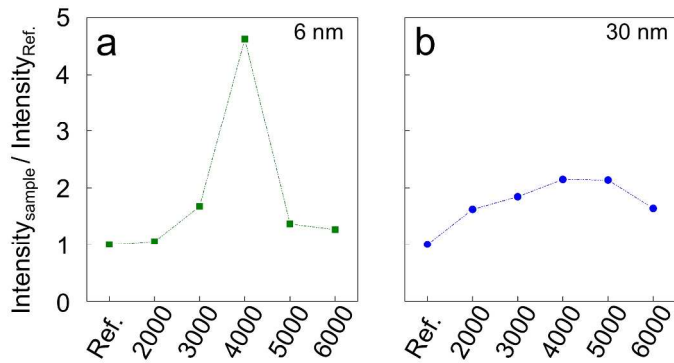


Figure S16. XRD intensity of the C₈-BTBT films with total thicknesses of a) 6 nm and b) 30 nm without and with spin-coated monolayers at different speeds.

As shown in **Figure S16a**, the 6 nm-thick film containing a monolayer as spin-coated at 4000 rpm showed a sharp peak with the highest intensity, approximately fivefold than that of the reference sample. Other samples of the spin-coated films also exhibited increased intensities as compared with the reference sample. Thus, the intensity presents an increase-then decrease trend along with the increasing speeds. Such a trend was consistent with that of device performance. It

thus indicates that a spin-coated crystalline monolayer can serve as an efficient template for further growth of evaporated molecules into high-quality crystalline films. Besides, we also performed the XRD measurements on C₈-BTBT bulk films with the thickness of 30 nm. A similar but much more moderate variation trend in the XRD intensity can be observed (Figure S16b). Hence, such a templating effect of the interfacial crystalline monolayers should mainly influence on the molecular packing behaviour for the first several evaporated monolayers.

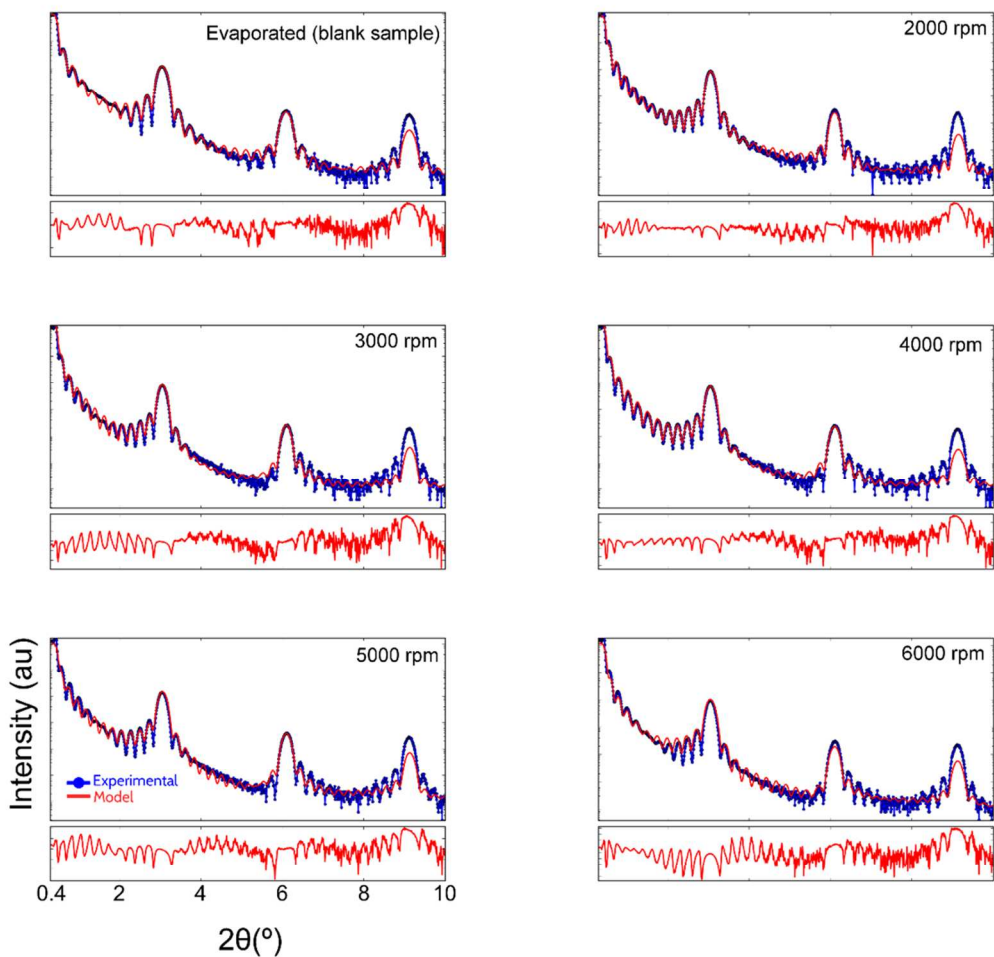


Figure S17. Experimental and multilayer model XRR traces for blank sample (only evaporated) and samples including predeposited spin coating layer at 2000-6000 rpm.

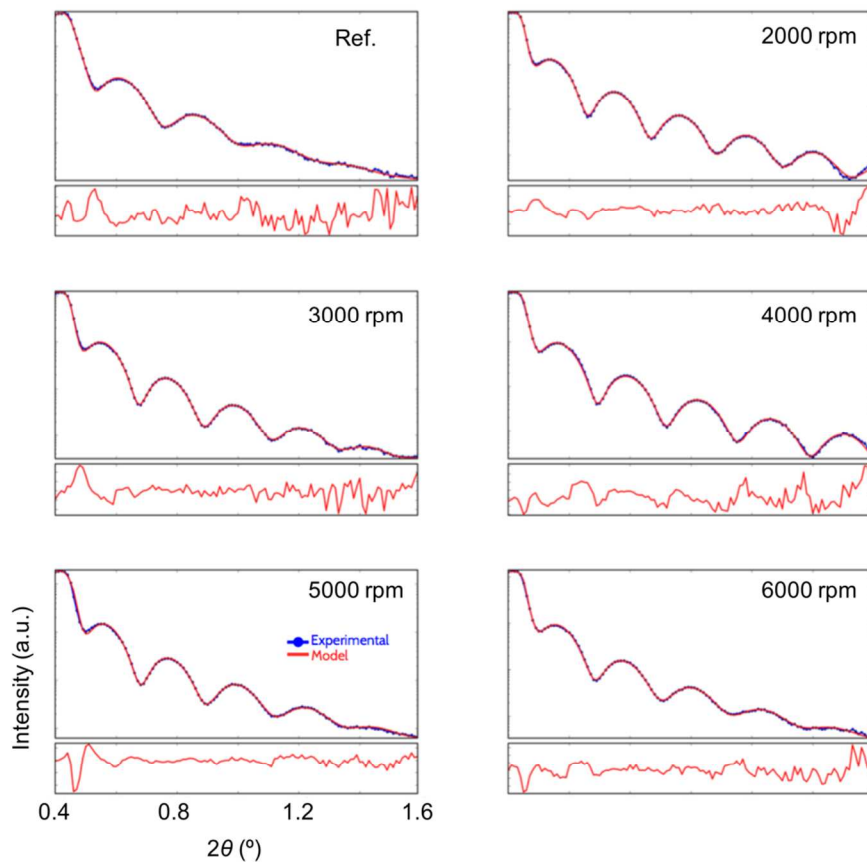


Figure S18. Experimental and theoretical fitting range $2\theta = 0.4^\circ$ to 1.6° of XRR traces for reference sample (only evaporated) and samples including predeposited spin coating layer at 2000-6000 rpm.

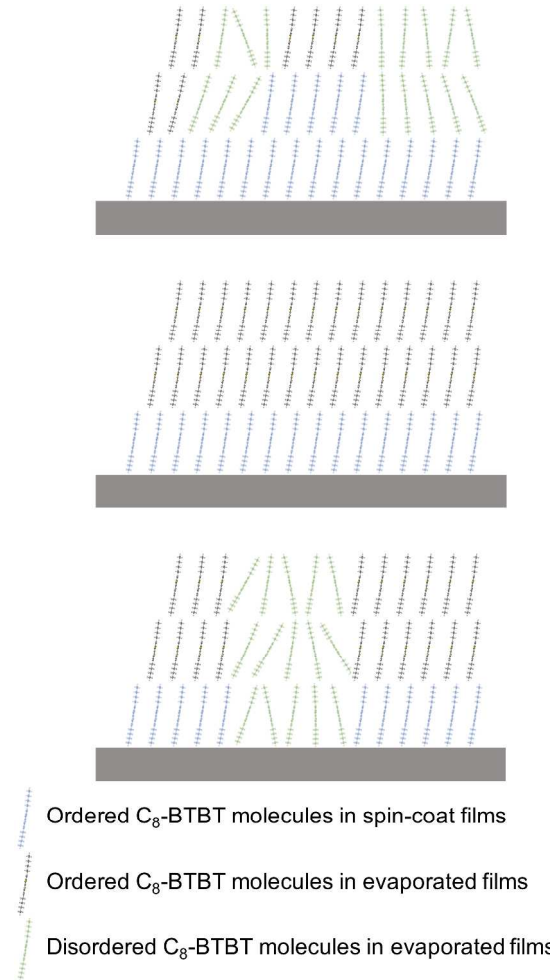


Figure S19. Schematic illustration of the C₈-BTBT film growth. (a) The islands existed in solution-processed C₈-BTBT films spin-coated at slow speeds will disrupt the molecular packing and induce disorders in upper films. (b) highly ordered molecular packing of C₈-BTBT on the spin-coated C₈-BTBT monolayers at 4000 rpm. (c) On spin-coated films at fast speed, the pinholes and cracks in this layer were filled by the evaporated molecules, exhibiting some disorder in the molecular packing.

The schematic representation regarding the growing mechanism of crystals has been added in the supporting information (**Figure S19**). On the solution-processed multilayers as spin-coated at relatively low speeds, the packing of evaporated C₈-BTBT molecules could be affected by the existing islands and their molecular orientations, resulting in disorders and discontinuity (Figure

S19a). When employing the uniform monolayer as spin-coated at an optimized speed of 4000 rpm, the evaporated C₈-BTBT molecules could pack into a highly ordered manner (Figure S19b). Further increase in the spin speed resulted in much discontinuous films with cracks and holes, thus impeding a highly ordered molecular packing during the following evaporation process (Figure S19c). Therefore, only monolayers deposited under optimized spin speed could serve as efficient templates for further growth of evaporated molecules into high-quality crystalline films. Besides, the blank sample without pre-deposited monolayer gave the most disordered thin-film, which is due to the lack of such a templating effect.

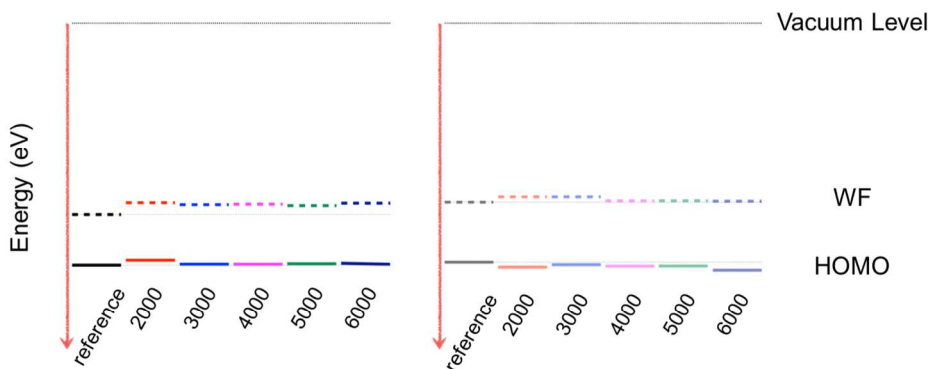


Figure S20. Energy level diagram of C₈-BTBT monolayers deposited by thermal evaporation and spin-coating (left) and hybrid-deposited C₈-BTBT films (right).

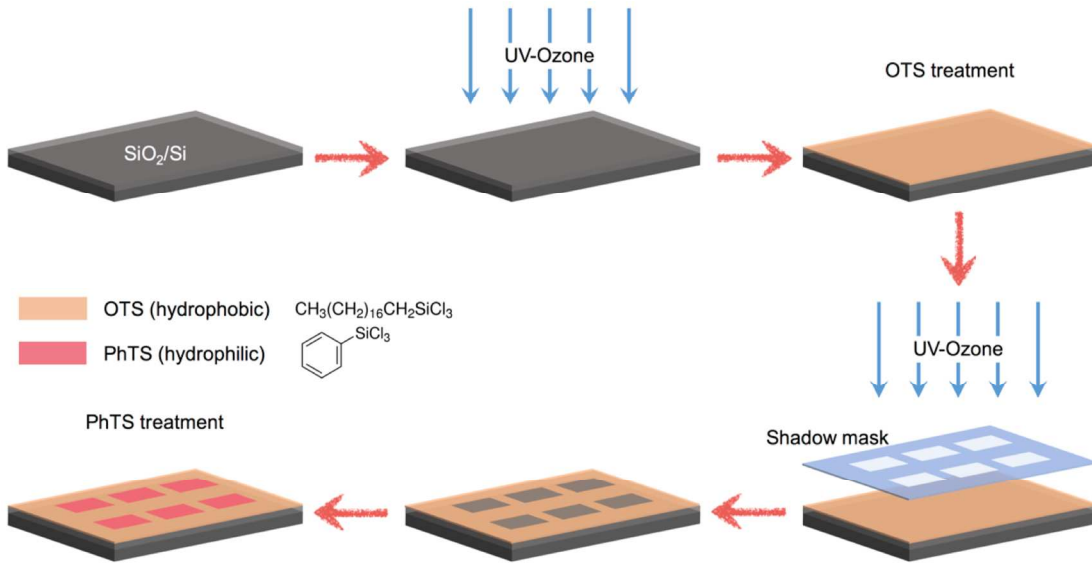


Figure S21. Fabrication process of patterned substrates treated by self-assembly molecules (OTS and PhTS).

Step 1. The substrates ($1.5 \times 1.5 \text{ cm}^2$) were cleaned by sequential sonication in acetone and isopropanol for 8 min each.

Step 2. The substrates were treated by UV-ozone for 15 min.

Step 3. The substrates underwent OTS treatment by immersion in a chloroform (CHCl_3) solution of trichloro(octadecyl)silane (OTS) (3 wt%) for 4 hours.

Step 4. The substrates were treated by UV-ozone with a shadow mask.

Step 5. The substrates underwent PhTS treatment by immersion in a toluene solution of phenyltrichlorosilane (PhTS) (3 wt%), which was then heated at 90°C for 15 hours in a glove box (N_2).

Step 6. The $\text{C}_8\text{-BTBT}$ films were deposited by spin-coating at a speed of 4000 rpm for 60 s.

Step 7. A protective layer was deposited by thermal evaporation with a shadow mask at a deposition rate of $\sim 0.1 \text{ \AA s}^{-1}$ and a base pressure of $\sim 10^{-4} \text{ Pa}$.

Step 8. The MoO_3 and Au electrodes were deposited using shadow masks.

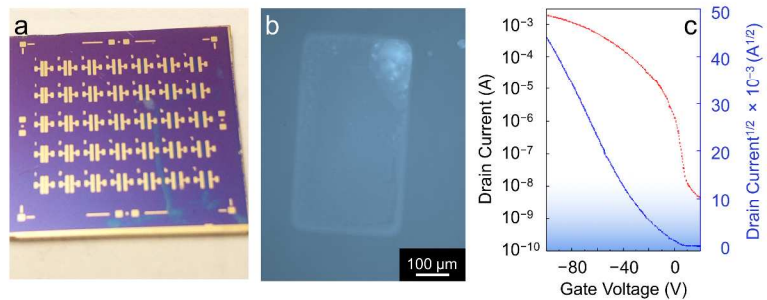


Figure S22. Optical microscopy images of a) transistor arrays and b) C₈-BTBT films on patterned substrates. c) Typical transfer curve of a device in the transistor array.

Table S1. Typical OFETs based on C₈-BTBT in literature.

Device structure	Dielectric	Average Mobility [cm ² V ⁻¹ s ⁻¹]	Maximum mobility [cm ² V ⁻¹ s ⁻¹]	Operating Voltage [V]	Ref.
BGTC	PVP	25	43	40	2
TGTC	Parylene C	16.4	31.3	60	3
BGTC	SiO ₂ /PMMA	3	9.1	40	4
BGTC	SiO ₂ /PS		3.56	40	5
TGBC	CYTOP	9.4	13	80	6
BGTC	SiO ₂ /ODTS		2.9	60	7
TGBC TGTC	CYTOP	5.5~5.7		40	8
TGBC	CYTOP/Polymer	7.9		40	9
BGTC	SiO ₂ /PMMA	3	9.1	40	10
BGTC	SiO ₂ /DTS	4~6		100	11
BGTC	SiO ₂ /OTS	9.2	10.4	60	12
BGTC	SiO ₂ /FTS	0.2~3.5	3.5	40	13
BGTC	SiO ₂ /OTS	2.6	6.9	40	14
TGBC	CYTOP	1.59	2.6	60	15
BGTC	SiO ₂		2.3	20	16
BGTC	SiO ₂ /PMMA		16	40	17
BGTC	SiO ₂ /BN		10	40	18
BGTC	SiO ₂ /HMDS	0.4	0.7	60	19
BGTC	SiO ₂ /PMMA	1.1	3.8	40	20
BGTC	SiO ₂	4.8	13	20	21
BGTC	AlO _x	4.7	9.8	4	22
BGTC	SiO ₂		16.0	80	23
BGTC	SiO ₂		18.2	100	24
BGTC	SiO ₂	9.8	11.3	100	This work

Table S2. Summary of electrical parameters of C₈-BTBT transistors.

Parameter	Reference	2000 rpm	3000 rpm	4000 rpm	5000 rpm	6000 rpm
Carrier Mobility (cm ² V ⁻¹ s ⁻¹)	1.5 ± 0.44	4.9 ± 0.38	5.5 ± 1.0	9.2 ± 0.96	8.9 ± 0.96	6.3 ± 1.2
On/off Ratio	2.6 × 10 ⁵	9.5 × 10 ⁵	1.6 × 10 ⁵	3.0 × 10 ⁵	2.6 × 10 ⁵	1.8 × 10 ⁵
Threshold Voltage (V)	– 39.6	– 15.6	– 27.5	– 16.2	– 12.7	– 25.0

Table S3. Lattice constants as obtained from theoretical fitting (Le-Bail) of C₈-BTBT films.

Sample	a (Å)	b (Å)	c (Å)	β (°)	Volume (Å ³)	Density (g/cm ³)
Single crystal	5.927 ± 0.007	7.88 ± 0.01	29.180 ± 0.004	92.443 ± 0.004	1362 ± 4	1.134 ± 0.003
Evaporation only	5.950 ± 0.007	7.91 ± 0.03	29.155 ± 0.012	91.8 ± 0.4	1371 ± 8	1.126 ± 0.006
2000 rpm	5.942 ± 0.007	7.93 ± 0.03	29.123 ± 0.008	90.9 ± 0.1	1372 ± 6	1.125 ± 0.005
3000 rpm	5.939 ± 0.007	7.84 ± 0.04	29.108 ± 0.008	92.1 ± 0.2	1355 ± 8	1.139 ± 0.007
4000 rpm	5.935 ± 0.009	7.73 ± 0.03	29.110 ± 0.010	92.2 ± 0.2	1335 ± 7	1.156 ± 0.006
5000 rpm	5.939 ± 0.009	7.92 ± 0.03	29.084 ± 0.009	90.8 ± 0.1	1367 ± 8	1.129 ± 0.007
6000 rpm	5.945 ± 0.007	7.91 ± 0.04	29.125 ± 0.010	91.5 ± 0.4	1369 ± 9	1.128 ± 0.007

Table S4. Summary of optimized parameters for multi-layered XRR model

Sample	C ₈ thickness (Å)	BTBT thickness (Å)	C ₈ density (FU/ Å ³)	BTBT density (FU/ Å ³)
Single crystal	20.13	8.9999	0.00186	0.00532
Evaporation only	16.5 ± 1.5	12.6 ± 1.5	0.0017 ± 0.0003	0.0061 ± 0.0004
2000 rpm	18.7 ± 1.6	10.3 ± 1.6	0.0021 ± 0.0003	0.0059 ± 0.0003
3000 rpm	19.0 ± 0.9	10.0 ± 1.0	0.0021 ± 0.0003	0.0051 ± 0.0002
4000 rpm	19.3 ± 0.5	9.6 ± 0.6	0.0022 ± 0.0003	0.0052 ± 0.0002
5000 rpm	17.7 ± 1.1	11.3 ± 1.1	0.0011 ± 0.0003	0.0058 ± 0.0007
6000 rpm	11.9 ± 0.6	17.1 ± 0.6	0.0016 ± 0.0004	0.0051 ± 0.0005

Reference:

- (1) Björck, M.; Andersson, G. GenX: an Extensible X-Ray Reflectivity Refinement Program Utilizing Differential Evolution. *J Appl Crystallogr* **2007**, *40*, 1174–1178.
- (2) Yuan, Y.; Giri, G.; Ayzner, A. L.; Zoombelt, A. P.; Mannsfeld, S. C. B.; Chen, J.; Nordlund, D.; Toney, M. F.; Huang, J.; Bao, Z. Ultra-High Mobility Transparent Organic Thin Film Transistors Grown by an Off-Centre Spin-Coating Method. *Nat. Commun.* **2014**, *5*, 1–9.
- (3) Minemawari, H.; Yamada, T.; Matsui, H.; Tsutsumi, J.; Haas, S.; Chiba, R.; Kumai, R.; Hasegawa, T. Inkjet Printing of Single-Crystal Films. *Nature* **2011**, *475*, 364–367.
- (4) Liu, C.; Minari, T.; Lu, X.; Kumatani, A.; Takimiya, K.; Tsukagoshi, K. Solution-Processable Organic Single Crystals with Bandlike Transport in Field-Effect Transistors. *Adv. Mater.* **2010**, *23*, 523–526.
- (5) Huang, Y.; Sun, J.; Zhang, J.; Wang, S.; Huang, H.; Zhang, J.; Yan, D.; Gao, Y.; Yang, J. Controllable Thin-Film Morphology and Structure for 2,7-Dioctyl[1]Benzothieno[3,2-B][1]Benzothiophene (C8BTBT) Based Organic Field-Effect Transistors. *Org. Electron.* **2016**, *36*, 73–81.
- (6) Paterson, A. F.; Treat, N. D.; Zhang, W.; Fei, Z.; Wyatt-Moon, G.; Faber, H.; Vourlias, G.; Patsalas, P. A.; Solomeshch, O.; Tessler, N.; et al. Small Molecule/Polymer Blend Organic Transistors with Hole Mobility Exceeding $13 \text{ Cm } 2\text{V}^{-1}\text{s}^{-1}$. *Adv. Mater.* **2016**, *28*, 7791–7798.
- (7) Izawa, T.; Miyazaki, E.; Takimiya, K. Molecular Ordering of High-Performance Soluble Molecular Semiconductors and Re-Evaluation of Their Field-Effect Transistor Characteristics. *Adv. Mater.* **2008**, *20*, 3388–3392.

- (8) Darmawan, P.; Minari, T.; Xu, Y.; Li, S.-L.; Song, H.; Chan, M.; Tsukagoshi, K. Optimal Structure for High-Performance and Low-Contact-Resistance Organic Field-Effect Transistors Using Contact-Doped Coplanar and Pseudo-Staggered Device Architectures. *Adv. Funct. Mater.* **2012**, *22*, 4577–4583.
- (9) Minari, T.; Kanehara, Y.; Liu, C.; Sakamoto, K.; Yasuda, T.; Yaguchi, A.; Tsukada, S.; Kashizaki, K.; Kanehara, M. Room-Temperature Printing of Organic Thin-Film Transistors with Π -Junction Gold Nanoparticles. *Adv. Funct. Mater.* **2014**, *24*, 4886–4892.
- (10) Minari, T.; Liu, C.; Kano, M.; Tsukagoshi, K. Controlled Self-Assembly of Organic Semiconductors for Solution-Based Fabrication of Organic Field-Effect Transistors. *Adv. Mater.* **2011**, *24*, 299–306.
- (11) Soeda, J.; Hirose, Y.; Yamagishi, M.; Nakao, A.; Uemura, T.; Nakayama, K.; Uno, M.; Nakazawa, Y.; Takimiya, K.; Takeya, J. Solution-Crystallized Organic Field-Effect Transistors with Charge-Acceptor Layers: High-Mobility and Low-Threshold-Voltage Operation in Air. *Adv. Mater.* **2011**, *23*, 3309–3314.
- (12) Kwon, S.; Kim, J.; Kim, G.; Yu, K.; Jo, Y.-R.; Kim, B.-J.; Kim, J.; Kang, H.; Park, B.; Lee, K. Organic Single-Crystal Semiconductor Films on a Millimeter Domain Scale. *Adv. Mater.* **2015**, *27*, 6870–6877.
- (13) Li, Y.; Liu, C.; Kumatori, A.; Darmawan, P.; Minari, T.; Tsukagoshi, K. Patterning Solution-Processed Organic Single-Crystal Transistors with High Device Performance. *AIP Advances* **2011**, *1*, 022149–7.

- (14) Xu, C.; He, P.; Liu, J.; Cui, A.; Dong, H.; Zhen, Y.; Chen, W.; Hu, W. A General Method for Growing Two-Dimensional Crystals of Organic Semiconductors by “Solution Epitaxy.” *Angew. Chem.* **2016**, *128*, 9671–9675.
- (15) Endo, T.; Nagase, T.; Kobayashi, T.; Takimiya, K.; Ikeda, M.; Naito, H. Solution-Processed Dioctylbenzothienobenzothiophene-Based Top-Gate Organic Transistors with High Mobility, Low Threshold Voltage, and High Electrical Stability. *Appl. Phys. Express* **2010**, *3*, 121601–121603.
- (16) Kano, M.; Minari, T.; Tsukagoshi, K. Improvement of Subthreshold Current Transport by Contact Interface Modification in P-Type Organic Field-Effect Transistors. *Appl. Phys. Lett.* **2009**, *94*, 143304–3.
- (17) Cho, J.-M.; Higashino, T.; Mori, T. Band-Like Transport Down to 20 K in Organic Single-Crystal Transistors Based on Dioctylbenzothienobenzothiophene. *Appl. Phys. Lett.* **2015**, *106*, 193303–193304.
- (18) He, D.; Zhang, Y.; Wu, Q.; Xu, R.; Nan, H.; Liu, J.; Yao, J.; Wang, Z.; Yuan, S.; Li, Y.; et al. Two-Dimensional Quasi-Freestanding Molecular Crystals for High-Performance Organic Field-Effect Transistors. *Nat. Commun.* **2014**, *5*, 1–7.
- (19) Wang, Y.; Chen, L.; Wang, Q.; Sun, H.; Wang, X.; Hu, Z.; Li, Y.; Shi, Y. Solution-Processed Organic Crystals Written Directly with a Rollerball Pen for Field-Effect Transistors. *Org. Electron.* **2014**, *15*, 2234–2239.

- (20) Kumatani, A.; Liu, C.; Li, Y.; Darmawan, P.; Takimiya, K.; Minari, T.; Tsukagoshi, K. Solution-Processed, Self-Organized Organic Single Crystal Arrays with Controlled Crystal Orientation. *Sci. Rep.* **2012**, *2*, 2411–2416.
- (21) Wang, Q.; Qian, J.; Li, Y.; Zhang, Y.; He, D.; Jiang, S.; Wang, Y.; Wang, X.; Pan, L.; Wang, J.; et al. 2D Single-Crystalline Molecular Semiconductors with Precise Layer Definition Achieved by Floating-Coffee-Ring-Driven Assembly. *Adv. Funct. Mater.* **2016**, *26*, 3191–3198.
- (22) Wang, Q.; Jiang, S.; Qian, J.; Song, L.; Zhang, L.; Zhang, Y.; Zhang, Y.; Wang, Y.; Wang, X.; Shi, Y.; et al. Low-Voltage, High-Performance Organic Field-Effect Transistors Based on 2D Crystalline Molecular Semiconductors. *Sci. Rep.* **2017**, *1*–8.
- (23) Zhang, Z.; Peng, B.; Ji, X.; Pei, K.; Chan, P. K. L. Marangoni-Effect-Assisted Bar-Coating Method for High-Quality Organic Crystals with Compressive and Tensile Strains. *Adv. Funct. Mater.* **2017**, *27*, 1703443–1703449.
- (24) Zhang, F.; Dai, X.; Zhu, W.; Chung, H.; Diao, Y. Large Modulation of Charge Carrier Mobility in Doped Nanoporous Organic Transistors. *Adv. Mater.* **2017**, *29*, 1700411–1700417.